

A time-fractional dual-phase-lag framework to investigate transistors with TMTC channels (TiS_3 , In_4Se_3) and size-dependent properties

Mohammad Hosein Fotovvat^a, Zahra Shomali^{b,*}, Jafar Ghazanfarian^a

^a*Mechanical Engineering Department, Faculty of Engineering, University of Zanjan, Zanjan, Iran*

^b*Department of Physics, Faculty of Basic Sciences, Tarbiat Modares University, Tehran, Iran*

Abstract

In this study, a time fractional dual-phase-lag model with temperature jump boundary condition as a choice for the Fourier's law replacement in thermal modeling of transistors, is utilized. In more details, the numerical simulation of heat transfer in newly proposed TMTC field effect transistors using fractional DPL equation has been investigated. Moreover, the Caputo fractional derivative is employed to formulate the finite difference scheme for discretization of the fractional DPL model. In order to obtain more precise results for the peak temperature rise, the temperature and heat flux profiles, the size-dependent thermal properties are taken into account. Also, the temperature jump boundary condition has been also applied by means of a mixed-type boundary condition. It is obtained that considering size-dependent thermal characteristics for transistors under study, results in increase of the peak temperature rise up to 250 percent. Furthermore, considering constant bulk thermal properties for the silicon MOSFET, certain oscillations are observed in the time-variation of the peak temperature rise for $\alpha = 0.7, 0.9$ and 1 . This presents the so-called negative bias temperature instability appearing in electronic nano-semiconductor devices. Finally, the hotspot temperature has been researched in transistors containing two-dimensional materials with quasi one-dimensional band structure channels. It is obtained that among the studied FETs, titanium trisulfide with maximum temperature increase

*Corresponding author, Tel.: +982182884785

Email address: shomali@modares.ac.ir (Zahra Shomali)

of 19.63 K exhibits the least peak temperature rise. This presents that TiS_3 may be an acceptable silicon channel replacement as far as the thermal issues are concerned.

Keywords: Nanoscale, heat conduction, dual-phase-lag, fractional calculus, 1D materials, field effect transistors

1. Introduction

The necessity for higher speed in constant power density, has decreased the size of the MOSFETs. New generation of transistors are built in sizes of less than 10 nm, in order to have more efficiency than that of the silicon-based transistors [1, 2]. On the contrary, as the size of the MOSFETs shrinks, they encounter imperfections and problems which disrupt their performance. Two-dimensional materials like graphene and transition metal dichalcogenide (TMD) with chemical composition of MX_2 (for example MoS_2), due to their reduced leakage current, are suitable candidates for use as the channel in field effect transistors [3]. However, excessive reduction of the channel dimensions in these transistors makes materials such as graphene to lose their perfect properties such as low weight and high mobility. Put differently, for two dimensional materials like graphene and transition metal dichalcogenides, reducing the system size to 10 nm or less, increases the edge effects and phonon edge scattering notably. These effects ruin the performance of the transistors [4]. With an eye toward solving this problem, one can utilize quasi one-dimensional materials for which the phonon scattering effect at edges is negligible. The two dimensional transition metal trichalcogenide materials (TMTCs) [5] with chemical composition of MX_3 such as TiS_3 and In_4X_3 as an instance In_4Se_3 , have quasi one-dimensional band structures and their energy gaps are about 5 eV. These quasi-one-dimensional materials have many optoelectronic properties of two-dimensional substances and also in addition has an advantage of imperceptible edge scattering effect [6]. Consequently, building a transistor with size less than 10 nm and higher reliability are more probable when one uses TMTCs instead of TMDCs or graphene-like materials.

On the other side, as the length scale of the electronic devices shrinks to the nanoscale, the classical equations of continuum mechanics fail to endorse the experimental data. Hence, it is necessary to develop creative models which predict more accurate results relative to the classical equations such as

Fourier's law with less computational cost and more simplicity. Meanwhile, the dual-phase-lag (DPL) model [7, 8] as a constitutive equation to investigate the non-Fourier heat transport in different cases of nanoscale MOSFETs has drawn attentions [9, 10, 11, 12, 13, 14, 15, 16, 17, 18, 19, 20, 21, 22]. As a consequence of the easiness, straightforwardness, adaptability, and preciseness of this method, it is a reliable choice for heat transfer investigation of transistors with disparate geometries. On the other hand, in recent years, the subject concerning combination of the fractional calculus and different diffusive models in order to investigate the anomalous diffusive phenomena considering the non-local, has been the center of attention. Indeed, fractional calculus has been successfully utilized for the modification of many existing models of physical phenomena. Actually, the theory of fractional derivatives and integral has been developed in the nineteenth century. Caputo and Mainardi have made use of fractional derivatives and found an adequate agreement between the obtained results and what has been found from the experiment [23, 24, 25]. In 2010, Sherief *et al.* presented the fractional single-phase-lagging for the sake of viscoelastic material behavior using the fractional calculus and Caputo fractional derivative. A satisfactory consistency between the numerical results obtained from the new suggested model and the available experimental data is seen [26]. Also, Mishra and Rai have formulated the fractional single-phase-lagging (FSPL) heat conduction equation via employing the single-phase lag model and Caputo fractional derivative [27]. In this study, the discretization has been performed using the compact difference scheme. Further, the non-Fourier heat conduction within a finite thin film under the effect of a time-varying and spatially-decaying laser heating considering the Dirichlet Boundary condition, has been investigated. In 2018, Ji *et al.* have established a fractional dual phase lag model based on the finite difference numerical method, to investigate the heat conduction in nanoscale devices [28]. Also, they have investigated the non-Fourier heat transport in a thin two-layer film exposed to the ultrashort-pulsed laser heating applying the fractional DPL model [29].

Here, in order to investigate reliability and functionality of the titanium trisulfide (TiS_3) and tetraindium triselenide (In_4Se_3) quasi one-dimensional transistors, as an alternative to the previous generation silicon transistors, temperature distribution profile and the maximum temperature increase in these transistors are investigated using the fractional DPL model. The heat transport through a silicon slab considering the temperature jump boundary condition, and in existence of the heat generation zone, is scrutinized. In

the present study, the heat conduction in MOSFETs will be investigated. In more details, first, the one-dimensional silicon MOSFETs will be investigated and the results will be used for verification. Then, the MOSFET containing silicon channel and buried oxide will be modeled using the fractional DPL. Then, the peak temperature rise and the temperature profile for quasi one-dimensional MOSFET transistors including newly proposed transition metal trichalcogenides gates, TiS_3 and In_4Se_3 , are studied using the fractional dual phase lag model. The MOSFET with maximum temperature increase of 19.63 K is found to have the least temperature rise. So, it can be suggested as the suitable replacement of the one-dimensional silicon channel. Moreover, the effect of size-dependent thermal conductivity on thermal behavior of the quasi-one-dimensional TMTC MOSFETs is studied.

The structure of present study is as follows. In Sec. 2, the governing equations, and the assumptions will be demonstrated. The numerical method is exhaustively discussed in Sec. 3. The validation results for different cases and the obtained results are given in Secs. 4 and 5. At last, the paper is concluded in Sec. 6.

2. Mathematical modeling

In this section, first, the derivation of fractional dual phase lag equation is presented. Then, the discretization of the governing equation, the way of applying the boundary condition, the initial conditions and the numerical finite difference scheme for discretization of the fractional DPL equation will be presented.

2.1. fractional DPL

The DPL model for the one-dimensional geometry is written as,

$$q(x, t + \tau_q) = -kT_x(x, t + \tau_t). \quad (1)$$

Where the q is the heat flux and T_x is the temperature gradient vector. The thermal conductivity is also presented as k . On the other hand, the differential relation for energy conservation law is:

$$\rho C_p T_t(x, t) = -q_x(x, t) + S(x, t). \quad (2)$$

Here ρ , C_p and $S(x, t)$, are respectively, the mass density, the specific heat and the heat source. The nanoscale heat transfer can be investigated

via DPL model using three methods. In the first method, the DPL equation is expanded using the Taylor series and then the heat flux is replaced utilizing the relation dragged out from the energy equation. Consequently, an equation containing only temperature as the unknown parameter is obtained [30, 9, 31]. Also, the unexpanded DPL and the energy equation can be simultaneously solved [32]. Dealing with the third method, the expanded DPL equation and the energy equation are together worked out to calculate the temperature profile and the heat flux [15]. When the thermal properties are temperature dependent, the equations are non-linear and one should use the third method. Here, the first method which considers the fractional Taylor expansion of the heat flux and the temperature gradient will be used:

$$\begin{aligned} q(x, t + \tau_q) &= q(x, t) + \frac{(\tau_q)^\alpha}{\Gamma(1 + \alpha)} {}_0^C D_t^\alpha q(x, t) + \dots \\ T_x(x, t + \tau_t) &= T_x(x, t) + \frac{(\tau_t)^\alpha}{\Gamma(1 + \alpha)} {}_0^C D_t^\alpha T_x(x, t) + \dots \end{aligned} \quad (3)$$

In the above equations, $0 < \alpha < 1$ and the ${}_0^C D_t^\alpha$ operator is the Caputo fractional derivative of order α [33]:

$${}_0^C D_t^\alpha f(t) = \frac{1}{\Gamma(1 - \alpha)} \int_0^t \frac{f'(\xi)}{(t - \xi)^\alpha} d\xi. \quad (4)$$

By substituting Eqs. (3) in Eq. (1), one can find the following relation:

$$q(x, t) + \frac{(\tau_q)^\alpha}{\Gamma(1 + \alpha)} {}_0^C D_t^\alpha q(x, t) = -k \left(T + \frac{(\tau_t)^\alpha}{\Gamma(1 + \alpha)} {}_0^C D_t^\alpha T \right)_x (x, t). \quad (5)$$

Taking the x-derivative of two sides of Eq. (1) along using the energy conservation law, the fractional DPL is obtained as:

$$\begin{aligned} \rho C_p \left[T_t + \frac{(\tau_q)^\alpha}{\Gamma(1 + \alpha)} {}_0^C D_t^\alpha T_t \right] (x, t) &= k \left(T + \frac{(\tau_t)^\alpha}{\Gamma(1 + \alpha)} {}_0^C D_t^\alpha T \right)_{xx} (x, t) \\ &+ f(x, t). \end{aligned} \quad (6)$$

Here, $f(x, t)$ is defined as

$$f(x, t) = S(x, t) + \frac{(\tau_q)^\alpha}{\Gamma(1 + \alpha)} {}_0^C D_t^\alpha S(x, t). \quad (7)$$

2.2. Non-dimensional governing equations

In order to make the governing equations (6) and (7) non-dimensional, the following non-dimensional parameters are defined:

$$\begin{aligned} u &= \frac{T - T_0}{T_0}, \quad q^* = \frac{q}{\rho C_p |v| T_0}, \quad t^* = [\Gamma(1 + \alpha)]^{1/\alpha} \frac{t}{\tau_q}, \\ x^* &= \frac{x}{L_c}, \quad Kn = \frac{\Lambda}{L_c}, \quad B = \frac{\tau_t}{\tau_q}. \end{aligned} \quad (8)$$

where, Λ , L_c , T , τ_q and v are, respectively, the phonon mean free-path, the characteristic length, the reference temperature, the heat flux phase lag for silicon with constant bulk thermal properties, and the energy carriers' average velocity (the sound speed). Also, the heat conduction coefficient of the solid material and the sound velocity are defined as $k = \rho C_p |v| \frac{\Lambda}{3}$ and $|v| = \Lambda / \tau_q$. By substituting the non-dimensional parameters and using the mentioned definitions, the non-dimensional fractional DPL equation is achieved:

$$\begin{aligned} \frac{\partial u}{\partial t^*} + {}_0^C D_{t^*}^{\alpha+1} u &= \frac{Kn^2}{3 [\Gamma(1 + \alpha)]^{1/\alpha}} \left[\frac{\partial^2 u}{\partial x^{*2}} + B {}_0^C D_{t^*}^\alpha \left(\frac{\partial^2 u}{\partial x^{*2}} \right) \right] \\ &+ F(x^*, t^*). \end{aligned} \quad (9)$$

It is easier to ignore the * sign and write the above equation in the following form:

$$\begin{aligned} u_t(x, t) + {}_0^C D_t^{\alpha+1} u(x, t) &= \frac{Kn^2}{3 [\Gamma(1 + \alpha)]^{1/\alpha}} \left(u + B {}_0^C D_t^\alpha u \right)_{xx}(x, t) \\ &+ F(x, t), \quad 0 \leq x \leq L, \quad 0 < t \leq \bar{T}. \end{aligned} \quad (10)$$

Also, $F(x, T)$ is defined as,

$$F(x, t) = \frac{\tau_q}{\rho C_p T_0 [\Gamma(1 + \alpha)]^{1/\alpha}} f(x, t). \quad (11)$$

The non-dimensional form of the Eqs. (2) and (5) are also presented as:

$$\begin{aligned}
u_t(x, t) &= -\frac{Kn}{[\Gamma(1 + \alpha)]^{1/\alpha}} q_x(x, t) + F(x, t), \\
&0 \leq x \leq L, \quad 0 < t \leq \bar{T} \\
q(x, t) + {}_0^C D_t^\alpha q(x, t) &= -\frac{Kn}{3} (u + B {}_0^{\alpha C} D_t^\alpha u)_x(x, t), \\
&0 \leq x \leq L, \quad 0 < t \leq \bar{T}. \quad (12)
\end{aligned}$$

2.3. Initial and boundary conditions

Using the boundary conditions considering no temperature jump, the phonon scattering effects are ignored. Hence, the numerical solutions obtained from the DPL model, especially near the boundaries, are not accurate and are different from the ones calculated using the Boltzmann equation. Actually, the important observed phenomenon dealing with the heat transfer in micro and nano dimensions, is the creation of temperature jump at the boundaries, and also its increase with decreasing the system size. This phenomenon can be modeled, using the mixed type boundary condition, $u_s - u_w = -\lambda Kn \frac{\partial u}{\partial \bar{n}}|_{\Omega}$, at the boundaries of the solution field. In this relation, u_s , u_w , n , Ω are, subsequently, the jumped temperature at the boundary, the boundary temperature, the unit vector normal to the boundary directed outward, and all the boundaries of the solution domain. Also, λ is a constant value, which should be determined. Using this boundary condition along the DPL model, makes the simulation of the temperature jump at the boundary more probable. The values of two unknown parameters of B and λ are determined such that the solution obtained from the DPL model, matches that of found from the Boltzmann equation, well. For a one-dimensional geometry, the temperature jump boundary conditions at the left and right boundaries are correspondingly established as:

$$\begin{aligned}
-\lambda Kn u_x(0, t) + u(0, t) &= \phi_1(t), \quad 0 < t \leq \bar{T} \\
\lambda Kn u_x(L, t) + u(L, t) &= \phi_2(t), \quad 0 < t \leq \bar{T}. \quad (13)
\end{aligned}$$

Moreover, the initial conditions are taken to be:

$$u(x, 0) = \psi_1(x), \quad u_t(x, 0) = \psi_2(x), \quad 0 \leq x \leq L. \quad (14)$$

3. Solution technique

In this section, we will discuss how one can discretize the one-dimensional fractional DPL equation with temperature jump boundary condition. So, the spatial interval $[0, L]$ is discretized into M subintervals, and also the temporal interval $[0, \bar{T}]$ is divided to K intervals:

$$\begin{aligned} h &= \frac{L}{M}, \quad x_i = ih, \quad 0 \leq i \leq M \\ \tau &= \frac{\bar{T}}{K}, \quad t_k = k\tau, \quad 0 \leq k \leq K. \end{aligned} \quad (15)$$

In this relations, h and τ are space and time steps. Further, as a mean to discretize the space and time derivatives, the following central finite difference operators are utilized:

$$\begin{aligned} \delta_x u_{i-\frac{1}{2}}^k &= \frac{1}{h} (u_i^k - u_{i-1}^k), \quad \delta_x^2 u_i^k = \frac{1}{h} \left(\delta_x u_{i+\frac{1}{2}}^k - \delta_x u_{i-\frac{1}{2}}^k \right) \\ \delta_t u_i^{k-\frac{1}{2}} &= \frac{1}{\tau} (u_i^k - u_i^{k-1}), \quad u_i^{k-\frac{1}{2}} = \frac{1}{2} (u_i^k + u_i^{k-1}). \end{aligned} \quad (16)$$

On the other hand, for the purpose of Caputo fractional derivative operator assessment, the $L - 1$ approximation is employed. For $0 < \alpha < 1$, this approximation leads to:

$$\begin{aligned} D_t^\alpha u_i^k &= \frac{\tau^{-\alpha}}{\Gamma(2-\alpha)} \left[a_0 u_i^k - \sum_{n=1}^{k-1} (a_{k-n-1} - a_{k-n}) u_i^n - a_{k-1} u_i^0 \right] \\ D_t^{\alpha+1} u_i^k &= \frac{\tau^{-\alpha}}{\Gamma(2-\alpha)} \left[a_0 \delta_t u_i^k - \sum_{n=1}^{k-1} (a_{k-n-1} - a_{k-n}) \delta_t u_i^n - a_{k-1} (u_t)_i^0 \right] \end{aligned} \quad (17)$$

The weighting factors are calculated via $a_l = (l+1)^{1-\alpha} - l^{1-\alpha}$, $l \geq 0$. In similarity to the Eqs. (17), in order to approximate the Caputo fractional

derivative in $k - 1/2$ time-step, the following relations are hold:

$$\begin{aligned}
D_t^\alpha u_i^{k-\frac{1}{2}} &= \frac{1}{2} (D_t^\alpha u_i^k + D_t^\alpha u_i^{k-1}) \\
&= \frac{\tau^{-\alpha}}{\Gamma(2-\alpha)} \left[a_0 u_i^{k-\frac{1}{2}} - \sum_{n=1}^{k-1} (a_{k-n-1} - a_{k-n}) u_i^{n-\frac{1}{2}} - a_{k-1} u_i^0 \right] \\
D_t^{\alpha+1} u_i^{k-\frac{1}{2}} &= \frac{1}{2} (D_t^{\alpha+1} u_i^k + D_t^{\alpha+1} u_i^{k-1}) \\
&= \frac{\tau^{-\alpha}}{\Gamma(2-\alpha)} \left[a_0 \delta_t u_i^{k-\frac{1}{2}} - \sum_{n=1}^{k-1} (a_{k-n-1} - a_{k-n}) \delta_t u_i^{n-\frac{1}{2}} - a_{k-1} (u_t)_i^0 \right]
\end{aligned}$$

Furthermore, the second-order derivative of an arbitrary function like $g(x)$ considering $g(x) \in C[x, x_M]$ is approximated contemplating the following equation,

$$\begin{aligned}
g_i'' &= \frac{1}{h^2} (g_{i+1} - 2g_i + g_{i-1}) = \delta_x^2 g_i \\
g_M'' &= \frac{2}{h} \left(g_M' - \frac{g_M - g_{M-1}}{h} \right) + \frac{h}{3} g_M''' \quad (18)
\end{aligned}$$

Besides, for an arbitrary function of $f(t)$ with the assumptions $f(t) \in C[t_{k-1}, t_k]$ and $t_{k-\frac{1}{2}}$, one has,

$$\frac{1}{2} (f'(t_{k-1}) + f'(t_k)) \simeq \frac{f(t_k) - f(t_{k-1})}{\tau} = \delta_t f^{k-\frac{1}{2}}. \quad (19)$$

Considering Eq. (10) in i -th node and using Eq. (18), the fractional DPL model for internal nodes are found as,

$$\frac{d}{dt} u_i(t) + {}_0^C D_t^{\alpha+1} u_i(t) = \frac{Kn^2}{3[\Gamma(1+\alpha)]^{1/\alpha}} \delta_x^2 (u_i(t) + B_0^{\alpha C} D_t^\alpha u_i(t)) \quad (20)$$

In the following, considering the above equation in k -th and $(k-1)$ -th time steps ($t = t_k$ and $t = t_{k-1}$), and taking the average of the two obtained equation and also using Eq. (19), the finite difference scheme for internal

nodes is achieved:

$$\begin{aligned} \delta_t u_i^{k-\frac{1}{2}} + {}_0^C D_t^{\alpha+1} u_i^{k-\frac{1}{2}} &= \frac{Kn^2}{3[\Gamma(1+\alpha)]^{1/\alpha}} \delta_x^2 \left(u_i^{k-\frac{1}{2}} + B_0^{\alpha C} D_t^\alpha u_i^{k-\frac{1}{2}} \right) \\ &+ F_i^{k-\frac{1}{2}}, \quad 1 \leq i \leq M-1, \quad 1 \leq k \leq K. \end{aligned} \quad (21)$$

Taking the x-derivative of two sides of the above equation and applying $x \rightarrow x_0$, the following relation is obtained:

$$\begin{aligned} \frac{Kn^2}{3[\Gamma(1+\alpha)]^{1/\alpha}} (u + B_0^{\alpha C} D_t^\alpha u)_{xxx}(x_0, t) &= u_{xt}(x_0, t) + {}_0^C D_t^{\alpha+1} u_x(x_0, t) \\ &- F_x(x_0, t). \end{aligned} \quad (22)$$

Also, contemplating Eq. (10) in the left boundary node (x, t) and using Eqs. (22), (18), and (13), the fractional DPL model for the left boundary node is found:

$$\begin{aligned} \left(1 + \frac{h}{3\lambda Kn} \right) \left(\frac{d}{dt} u_0(t) + {}_0^C D_t^{\alpha+1} u_0(t) \right) &= \frac{2Kn^2}{3h[\Gamma(1+\alpha)]^{1/\alpha}} \delta_x \left(u_{\frac{1}{2}}(t) + B_0^{\alpha C} D_t^\alpha u_{\frac{1}{2}}(t) \right) \\ &- \frac{2Kn}{3h\lambda[\Gamma(1+\alpha)]^{1/\alpha}} (u_0(t) + B_0^{\alpha C} D_t^\alpha u_0(t)) + W_0(t). \end{aligned} \quad (23)$$

Here, $W_0(t)$ is defined as,

$$\begin{aligned} W_0(t) &= \frac{2Kn}{3h\lambda[\Gamma(1+\alpha)]^{1/\alpha}} (\phi_1(t) + B_0^{\alpha C} D_t^\alpha \phi_1(t)) \\ &+ \frac{h}{3\lambda Kn} \left(\frac{d}{dt} \phi_1(t) + {}_0^C D_t^{\alpha+1} \phi_1(t) \right) + \frac{h}{3} (F_x)_0(t) + F_0(t). \end{aligned} \quad (24)$$

In the next step, with consideration of Eq. (23) in k-th time-step ($t = t_k$) and (k-1)-th time-step ($t = t_{k-1}$), and averaging the two obtained equation, and also using Eq. (19), the finite difference scheme for the left boundary

node is obtained,

$$\begin{aligned} & \left(1 + \frac{h}{3\lambda Kn}\right) \left(\delta_t u_0^{k-\frac{1}{2}} + {}^C D_t^{\alpha+1} u_0^{k-\frac{1}{2}}\right) = \frac{2Kn^2}{3h[\Gamma(1+\alpha)]^{1/\alpha}} \delta_x \left(u_{\frac{1}{2}}^{k-\frac{1}{2}} + B_0^{\alpha C} D_t^\alpha u_{\frac{1}{2}}^{k-\frac{1}{2}}\right) \\ & - \frac{2Kn}{3h\lambda[\Gamma(1+\alpha)]^{1/\alpha}} \left(u_0^{k-\frac{1}{2}} + B_0^{\alpha C} D_t^\alpha u_0^{k-\frac{1}{2}}\right) + W_0^{k-\frac{1}{2}}, \quad 1 \leq k \leq K. \end{aligned} \quad (25)$$

In the above relation, $W_0^{k-\frac{1}{2}}$ is,

$$\begin{aligned} W_0^{k-\frac{1}{2}} &= \frac{2Kn}{3h\lambda[\Gamma(1+\alpha)]^{1/\alpha}} \left(\phi_1^{k-\frac{1}{2}} + B_0^{\alpha C} D_t^\alpha \phi_1^{k-\frac{1}{2}}\right) \\ &+ \frac{h}{3\lambda Kn} \left(\frac{d}{dt} \phi_1^{k-\frac{1}{2}} + {}^C D_t^{\alpha+1} \phi_1^{k-\frac{1}{2}}\right) + \frac{h}{3} (F_x)_0^{k-\frac{1}{2}} + F_0^{k-\frac{1}{2}}. \end{aligned} \quad (26)$$

Similarly, repeating the above discretization method, one acquires the finite difference scheme for the right boundary node,

$$\begin{aligned} & \left(1 + \frac{h}{3\lambda Kn}\right) \left(\delta_t u_M^{k-\frac{1}{2}} + {}^C D_t^{\alpha+1} u_M^{k-\frac{1}{2}}\right) \\ &= -\frac{2Kn^2}{3h[\Gamma(1+\alpha)]^{1/\alpha}} \delta_x \left(u_{M-\frac{1}{2}}^{k-\frac{1}{2}} + B_0^{\alpha C} D_t^\alpha u_{M-\frac{1}{2}}^{k-\frac{1}{2}}\right) \\ &- \frac{2Kn}{3h\lambda[\Gamma(1+\alpha)]^{1/\alpha}} \left(u_M^{k-\frac{1}{2}} + B_0^{\alpha C} D_t^\alpha u_M^{k-\frac{1}{2}}\right) + W_M^{k-\frac{1}{2}}, \quad 1 \leq k \leq K. \end{aligned} \quad (27)$$

Where, $W_M^{k-\frac{1}{2}}$ is calculated through,

$$\begin{aligned} W_M^{k-\frac{1}{2}} &= \frac{2Kn}{3h\lambda[\Gamma(1+\alpha)]^{1/\alpha}} \left(\phi_2^{k-\frac{1}{2}} + B_0^{\alpha C} D_t^\alpha \phi_2^{k-\frac{1}{2}}\right) \\ &+ \frac{h}{3\lambda Kn} \left(\frac{d}{dt} \phi_2^{k-\frac{1}{2}} + {}^C D_t^{\alpha+1} \phi_2^{k-\frac{1}{2}}\right) - \frac{h}{3} (F_x)_M^{k-\frac{1}{2}} + F_M^{k-\frac{1}{2}}. \end{aligned} \quad (28)$$

The presented finite difference scheme for the fractional DPL model with temperature jump boundary condition, is unconditionally stable and convergent. The order of convergence based on the infinity norm, is the order of $2 - \alpha$ and 2, respectively, on time and space [28]. When the Caputo fractional derivative operator approximation is placed in Eqs. (21), (25), and

(27), the finite difference discretized form of the fractional DPL model with temperature jump boundary condition is achieved,

$$\begin{aligned}
& (d_1 c_1 + 2d_2 c_2 + d_3 c_3) u_0^k + (-2d_2 c_2) u_1^k = (d_1 c_1 - 2d_2 c_2 - d_3 c_3) u_0^{k-1} \\
& + (2d_2 c_2) u_1^{k-1} + c_1 \mu \left[\sum_{n=1}^{k-1} (a_{k-n-1} - a_{k-n}) \left(\frac{u_0^n - u_0^{n-1}}{\tau} \right) + a_{k-1} (\psi_2)_0 \right] \\
& - \frac{2}{h} B^\alpha \mu c_2 \left[\sum_{n=1}^{k-1} (a_{k-n-1} - a_{k-n}) \left(\frac{u_1^n + u_1^{n-1} - u_0^n - u_0^{n-1}}{2h} \right) + a_{k-1} \left(\frac{u_1^0 - u_0^0}{h} \right) \right] \\
& + \frac{2}{h\lambda} B^\alpha \mu c_3 \left[\sum_{n=1}^{k-1} (a_{k-n-1} - a_{k-n}) \left(\frac{u_0^n + u_0^{n-1}}{2} \right) + a_{k-1} u_0^0 \right] + \frac{2}{h\lambda} c_3 \left\{ \frac{\phi_1^k + \phi_1^{k-1}}{2} \right. \\
& + B^\alpha \mu \left[\frac{a_0}{2} (\phi_1^k + \phi_1^{k-1}) - \sum_{n=1}^{k-1} (a_{k-n-1} - a_{k-n}) \left(\frac{\phi_1^n + \phi_1^{n-1}}{2} \right) - a_{k-1} \phi_1^0 \right] \left. \right\} \\
& + \frac{h}{3\lambda K n} \left\{ \frac{\phi_1^k - \phi_1^{k-1}}{\tau} + \mu \left[\frac{a_0}{\tau} (\phi_1^k - \phi_1^{k-1}) - \sum_{n=1}^{k-1} (a_{k-n-1} - a_{k-n}) \left(\frac{\phi_1^n - \phi_1^{n-1}}{\tau} \right) \right. \right. \\
& \left. \left. - a_{k-1} (\phi_1)_t^0 \right] \right\} + \frac{h}{3} \left(\frac{(F_x)_0^k + (F_x)_0^{k-1}}{2} \right) + \frac{F_0^k + F_0^{k-1}}{2}, \quad 1 \leq k \leq K. \quad (29)
\end{aligned}$$

$$\begin{aligned}
& (-d_2c_2) u_{i+1}^k (d_1 + 2d_2c_2) u_i^k + (-d_2c_2) u_{i-1}^k = (d_1 - 2d_2c_2) u_i^{k-1} \\
& + d_2c_2 (u_{i+1}^{k-1} + u_{i-1}^{k-1}) + \mu \left[\sum_{n=1}^{k-1} (a_{k-n-1} - a_{k-n}) \left(\frac{u_i^n - u_i^{n-1}}{\tau} \right) + a_{k-1}(\psi_2)_i \right] \\
& - B^\alpha \mu c_2 \left[\sum_{n=1}^{k-1} (a_{k-n-1} - a_{k-n}) \left(\frac{u_{i+1}^n + u_{i+1}^{n-1} - 2u_i^n - 2u_i^{n-1} + u_{i-1}^n + u_{i-1}^{n-1}}{2h^2} \right) \right. \\
& \left. + a_{k-1} \left(\frac{u_{i+1}^0 - 2u_i^0 + u_{i-1}^0}{h^2} \right) \right] \Bigg\} + \frac{F_i^k + F_i^{k-1}}{2}, \quad 1 \leq i \leq M-1, \quad 1 \leq k \leq K
\end{aligned} \tag{30}$$

$$\begin{aligned}
& (d_1c_1 + 2d_2c_2 + d_3c_3) u_M^k + (-2d_2c_2) u_{M-1}^k = (d_1c_1 - 2d_2c_2 - d_3c_3) u_M^{k-1} \\
& + (2d_2c_2) u_{M-1}^{k-1} + c_1 \mu \left[\sum_{n=1}^{k-1} (a_{k-n-1} - a_{k-n}) \left(\frac{u_M^n - u_M^{n-1}}{\tau} \right) + a_{k-1}(\psi_2)_M \right] \\
& + \frac{2}{h} B^\alpha \mu c_2 \left[\sum_{n=1}^{k-1} (a_{k-n-1} - a_{k-n}) \left(\frac{u_M^n + u_M^{n-1} - u_{M-1}^n - u_{M-1}^{n-1}}{2h} \right) + a_{k-1} \left(\frac{u_M^0 - u_{M-1}^0}{h} \right) \right] \\
& + \frac{2}{h\lambda} B^\alpha \mu c_3 \left[\sum_{n=1}^{k-1} (a_{k-n-1} - a_{k-n}) \left(\frac{u_M^n + u_M^{n-1}}{2} \right) + a_{k-1} u_M^0 \right] + \frac{2}{h\lambda} c_3 \left\{ \frac{\phi_2^k + \phi_2^{k-1}}{2} \right. \\
& \left. + B^\alpha \mu \left[\frac{a_0}{2} (\phi_2^k + \phi_2^{k-1}) - \sum_{n=1}^{k-1} (a_{k-n-1} - a_{k-n}) \left(\frac{\phi_2^n + \phi_2^{n-1}}{2} \right) - a_{k-1} \phi_2^0 \right] \right\} \\
& + \frac{h}{3\lambda Kn} \left\{ \frac{\phi_2^k - \phi_2^{k-1}}{\tau} + \mu \left[\frac{a_0}{\tau} (\phi_2^k - \phi_2^{k-1}) - \sum_{n=1}^{k-1} (a_{k-n-1} - a_{k-n}) \left(\frac{\phi_2^n - \phi_2^{n-1}}{\tau} \right) \right. \right. \\
& \left. \left. - a_{k-1} (\phi_2)_t^0 \right] \right\} - \frac{h}{3} \left(\frac{(F_x)_M^k + (F_x)_M^{k-1}}{2} \right) + \frac{F_M^k + F_M^{k-1}}{2}, \quad 1 \leq k \leq K \tag{31}
\end{aligned}$$

In the relations above, μ , d_1 , d_2 , d_3 , c_1 , c_2 and c_3 are defined as,

$$\begin{aligned}
\mu &= \frac{\tau^{-\alpha}}{\Gamma(2-\alpha)}, \quad d_1 = \frac{\mu a_0 + 1}{\tau}, \quad d_2 = \frac{B^\alpha \mu a_0 + 1}{2h^2}, \quad d_3 = \frac{B^\alpha \mu a_0 + 1}{h\lambda}, \\
c_1 &= 1 + \frac{h}{3\lambda Kn}, \quad c_2 = \frac{Kn^2}{3[\Gamma(1+\alpha)]^{1/\alpha}}, \quad c_3 = \frac{Kn}{3[\Gamma(1+\alpha)]^{1/\alpha}}.
\end{aligned} \tag{32}$$

4. Verification

In this section, first, in order to test the accuracy of the presented finite difference scheme, five different one-dimensional cases with the temperature jump boundary condition and a source heat are investigated. The obtained results including the convergence order and the error in base of the infinity norm, are verified with the available data in [28] to be sure of accuracy of the derived procedure. Then, the results of heat transport investigation in the newly proposed quasi one-dimensional transistors will be presented. The geometry of cases which are studied in the present work are shown in Fig. 1. Also, the verifications performed for different cases and the results obtained from various states of MOSFET transistors are all gathered in Table. 1.

Table 1: Details of different cases for validation and results.

Verification cases				
Type of transistor	Channel material	Heat generation	Buried oxide	bulk/film properties
Case one	-	Entire transistor	No	Bulk
Case two	-	Entire transistor	No	Bulk
Case three	Si	The beginning	No	Bulk
Case four	-	No	No	Bulk
Case five	Si	No	No	Bulk
Final results				
Type of transistor	Channel material	Heat generation	Buried oxide	bulk/film properties
Case I(a)	Si	The beginning	No	Bulk
Case I(b)	Si	The beginning	No	Film
Case II(a)	Si	The beginning	Yes	Bulk
Case II(b)	Si	The beginning	Yes	Film
Case III	Si	The middle	No	Film
Case IV	$TiS - 3$	The middle	No	Film
Case V	$In4Se3$	The middle	No	Film

4.1. Mesh/time-step size independence tests

The results of the time/step size independence test for the first geometry, Fig. 1(a), are demonstrated in Table. 2. The results are shown for three

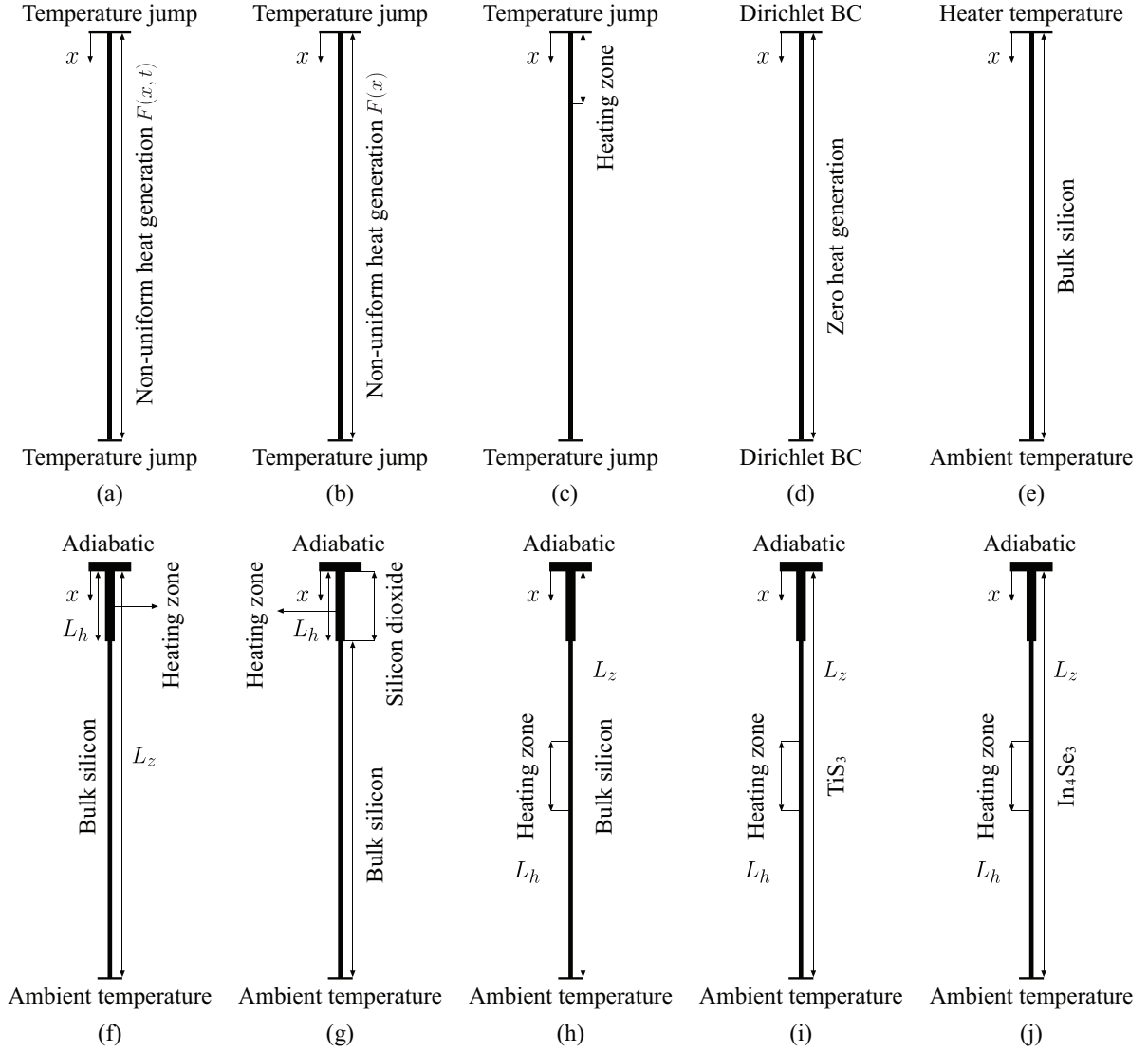


Figure 1: Schematic geometry and corresponding boundary conditions of different modeled transistors, (a) the slab with non-uniform heat generation as a function of time and space, (b) the slab with non-uniform heat generation as a function of space, (c) the silicon slab with uniform heat generation at the upper part, (d) the slab without the source term, (e) the silicone slab without the source term, (f) the silicone MOSFET with uniform heat generation at the upper part, (g) the MOSFET with the buried oxide with uniform heat generation, (h) the silicon MOSFET with uniform heat generation at the middle part, (i) the TiS_3 MOSFET with uniform heat generation at the middle part, (j) the In_4Se_3 MOSFET with uniform heat generation at the middle part.

different temperatures and also for five values of position. It is found that the results for the meshes of (M=2000, K=3000) and (M=2200, K=3200) are similar. Hence, to reduce the computational cost, the mesh, M=2000, K=3000, is used to proceed the modeling.

Table 2: Results of the mesh size and the time-step size independence tests at $t = 10$ ps.

(M, K)	$x = 0$ nm	$x = 10$ nm	$x = 20$ nm	$x = 30$ nm	$x = 40$ nm	$x = 50$ nm
(1000, 2000)	307.2538	304.5218	300.9154	300.0286	300.0000	300.0000
(1200, 2200)	307.2537	304.5195	300.9144	300.0285	300.0000	300.0000
(1400, 2400)	307.2536	304.5179	300.9137	300.0284	300.0000	300.0000
(1600, 2600)	307.2536	304.5166	300.9132	300.0284	300.0000	300.0000
(1800, 2800)	307.2536	304.5157	300.9127	300.0283	300.0000	300.0000
(2000, 3000)	307.2535	304.5149	300.9124	300.0283	300.0000	300.0000
(2200, 3200)	307.2535	304.5142	300.9121	300.0283	300.0000	300.0000

4.2. Verification: Case one

Here, the one-dimensional fractional DPL model for the case containing the temperature jump boundary condition and the non-homogeneous heat source, which is presented in Fig. 1(a), is studied. The governing equation, the boundary and initial conditions for this case are respectively as,

$$\begin{aligned}
u_t(x, t) + {}_0^C D_t^{\alpha+1} u(x, t) &= \frac{Kn^2}{3[\Gamma(1+\alpha)]^{1/\alpha}} (u + B_0^{\alpha C} D_t^\alpha u)_{xx}(x, t) \\
&+ F(x, t), \quad 0 \leq x \leq 1, \quad 0 < t \leq 1
\end{aligned} \tag{33}$$

$$\begin{aligned}
-\lambda Knu_x(0, t) + u(0, t) &= -\pi\lambda Knt^3, \quad 0 < t \leq 1 \\
\lambda Knu_x(1, t) + u(1, t) &= -\pi\lambda Knt^3, \quad 0 < t \leq 1 \\
u(x, 0) = 0, \quad u_t(x, 0) &= 0, \quad 0 \leq x \leq 1
\end{aligned} \tag{34}$$

The considered source heat $F(x, t)$ is,

$$F(x, t) = \left[3t^2 + \frac{6}{\Gamma(3 - \alpha)} t^{2-\alpha} + \frac{\pi^2 Kn^2}{3[\Gamma(1 + \alpha)]^{1/\alpha}} \left(t^3 + \frac{6B^\alpha}{\Gamma(4 - \alpha)} t^{3-\alpha} \right) \right] \sin(\pi x) \quad (35)$$

Also, the analytical solution is found to be $U(x, t) = t^3 \sin(\pi x)$ [28]. The following relations are used to calculate the numerical errors in base of the infinity norm and the convergence order,

$$E_\infty(h) = \|U^K - u^K\|_\infty$$

$$Rate_1 = \log_2 \left(\frac{E_\infty(2h)}{E_\infty(h)} \right). \quad (36)$$

In order to find the convergence order, the time interval is divided into $K = \bar{T}(\frac{M}{L})^{\frac{2}{2-\alpha}}$ subintervals. In Tab. 3, our obtained results using the infinity norm and the convergence order are compared with those calculated by Ji *et al.*[28] for $Kn = \frac{2}{\pi} < 1$, $\lambda = \frac{1}{5}$, $B = \frac{1}{2}$, and different values of α . Also, analogously,

Table 3: The infinity norm and the convergence order for $Kn = \frac{2}{\pi} < 1$.

Ji et al. [28]		Present results		h	α
$E_\infty(h)$	$Rate_1$	$E_\infty(h)$	$Rate_1$		
	1.637×10^{-3}		1.840×10^{-3}	0.05	0.3
2.012	4.057×10^{-4}	2.001	4.597×10^{-4}	0.025	
1.997	1.016×10^{-4}	1.998	1.151×10^{-4}	0.0125	
2.010	2.522×10^{-5}	1.994	2.890×10^{-5}	0.00625	
	1.982×10^{-3}		2.112×10^{-3}	0.05	0.5
2.015	4.902×10^{-4}	1.981	5.349×10^{-4}	0.025	
2.002	1.224×10^{-4}	1.999	1.338×10^{-4}	0.0125	
2.001	3.057×10^{-5}	1.999	3.346×10^{-5}	0.00625	
	2.380×10^{-3}		2.477×10^{-3}	0.05	0.7
2.009	5.913×10^{-4}	1.993	6.223×10^{-4}	0.025	
1.998	1.480×10^{-4}	1.998	1.558×10^{-4}	0.0125	
2.000	3.700×10^{-5}	2.000	3.894×10^{-5}	0.00625	

the numerical results comparison for the parameters $Kn = \frac{4}{\pi} < 1$, $\lambda = \frac{1}{10}$,

and $B = \frac{4}{3}$ are displayed in Tab. 4. According to Tabs. 3 and 4, as one expects, the convergence order goes to $O(h^2)$, and also as time and space steps decrease, the value of the numerical error based on the infinity norm reduces. As it is shown in Tab. 3, the average relative error between our results and the one reported in [28], for the infinity norm error and the convergence error at $Kn = \frac{2}{\pi} < 1$ are, subsequently, 9 and 0.5 percent. Also, the Tab. 4 demonstrates that the obtained errors when $Kn = \frac{4}{\pi} > 1$ holds, are less than 20 and 0.5 percent. Moreover, comparison between the analytical results and the numerical data obtained from the finite difference scheme is shown in Fig. 2. It is seen that the numerical results corresponding to $Kn = \frac{2}{\pi}$ and $Kn = \frac{4}{\pi}$ for $\alpha = 0.7$ present acceptable consistency with the analytical results, and the average relative error for both results is less than one percent.

Table 4: The infinity norm and the rate of convergence for $Kn = \frac{4}{\pi} > 1$.

Ji et al. [28]		Present results		h	α
$E_\infty(h)$	$Rate_1$	$E_\infty(h)$	$Rate_1$		
	2.498×10^{-3}		3.013×10^{-3}	0.05	0.3
1.985	6.309×10^{-4}	1.977	7.654×10^{-4}	0.025	
1.981	1.598×10^{-4}	1.980	1.939×10^{-4}	0.0125	
1.993	4.016×10^{-5}	1.981	4.912×10^{-5}	0.00625	0.5
	3.087×10^{-3}		3.645×10^{-3}	0.05	
1.997	7.732×10^{-4}	1.972	9.289×10^{-4}	0.025	
1.993	1.943×10^{-4}	1.990	2.339×10^{-4}	0.0125	0.7
1.995	4.873×10^{-5}	1.993	5.873×10^{-5}	0.00625	
	3.685×10^{-3}		4.323×10^{-3}	0.05	
2.002	9.200×10^{-4}	1.989	1.089×10^{-3}	0.025	0.7
1.997	2.306×10^{-4}	1.996	2.730×10^{-4}	0.0125	
1.999	5.768×10^{-5}	1.999	6.832×10^{-5}	0.00625	

4.3. Verification: Case two

In this section, the case presented in Fig. 1(b) has been investigated. Due to the lack of analytical solutions, the maximum numerical error and

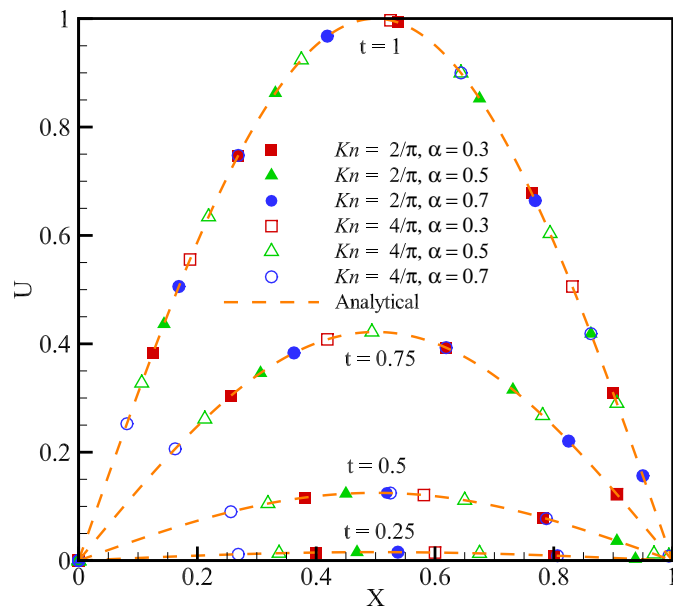


Figure 2: Comparison of analytical and numerical results of Ji *et al.* [28] considering the case 1 for different values of α , $h=0.00625$, and $\tau=0.001$.

convergence error are calculated via,

$$H_\infty(h) = \max \left| u_i^K(h, \tau) - u_{2i}^{2K} \left(\frac{h}{2}, \frac{\tau}{2} \right) \right|, \quad 0 \leq i \leq M$$

$$Rate_2 = \log_2 \left(\frac{H_\infty(2h)}{H_\infty(h)} \right) \quad (37)$$

Here, the governing equation and the boundary equations are described respectively, by Eqs. (10), (13), and (14). The maximum numerical error and the convergence order for this case when $\bar{T} = 1$, $L = 1$, $B = 0.25$, $\lambda = 1$, $\phi_1(t) = 0$, $\phi_2(t) = 2$, $\psi_1 = 0$, $\psi_2 = 0$, $F(x, t) = \sin(x)$, and $Kn = 10$. The obtained results are dispensed in Tab. 5. As the results suggest, as the space

Table 5: Error analysis and the convergence order at $Kn = 10$.

Ji et al. [28]		Present results		h	α
$H_\infty(h)$	$Rate_2$	$H_\infty(h)$	$Rate_2$		
	8.262×10^{-6}		5.698×10^{-6}	0.05	0.3
2.225	1.767×10^{-6}	2.261	1.189×10^{-6}	0.025	
2.110	4.093×10^{-7}	2.089	2.796×10^{-7}	0.0125	
2.089	9.623×10^{-8}	2.046	6.769×10^{-8}	0.00625	
	3.429×10^{-6}		3.819×10^{-6}	0.05	0.5
2.326	6.837×10^{-7}	2.195	8.340×10^{-7}	0.025	
2.279	1.409×10^{-7}	2.125	1.912×10^{-7}	0.0125	
2.208	3.050×10^{-8}	2.086	4.502×10^{-8}	0.00625	
	9.569×10^{-6}		6.985×10^{-6}	0.05	0.7
1.938	2.498×10^{-6}	1.882	1.895×10^{-6}	0.025	
1.954	6.447×10^{-7}	1.950	4.903×10^{-7}	0.0125	
1.977	1.638×10^{-7}	1.982	1.241×10^{-7}	0.00625	

and time steps decrease, the value of the maximum numerical error reduces and the convergence order goes to $O(h^2)$.

4.4. Verification: Case three

Here, thermal analysis of a silicon slab with uniform heat generation zone and temperature jump boundary condition like what presented in Fig. 1 has been performed using a fractional DPL model. The thermal properties of silicon are presented in Tab. 6. Again, the governing equation and the

Table 6: Thermal properties of silicon [9]

$\rho C_p(\text{ Jm}^{-3}\text{K}^{-1})$	$\tau_q(\text{ps})$	$L_z(\text{nm})$	$\Lambda(\text{nm})$	$L_c(\text{nm})$	$T_0(\text{K})$
1.5×10^6	33.33	50	100	10	300

boundary equations are presented, respectively, by Eqs. (10), (13), and (14). Also, the heat source is considered as,

$$f(x, t) = \begin{cases} 10^{19} \text{ (Js}^{-1}\text{m}^{-3}\text{)}, & 0 \leq x \leq \frac{L_z}{5L_c}, \quad 0 \leq t \leq \bar{T} \\ 0, & \frac{L_z}{5L_c} < x \leq \frac{L_z}{L_c}, \quad 0 \leq t \leq \bar{T} \end{cases} \quad (38)$$

In order to numerically investigate the problem, parameters $B = 0.05$, $Kn = 10$ and $\lambda = \sqrt{0.0037 + 0.4022e^{-Kn}}$ are taken from Ghazanfarian and Abbassi [30]. Also $\phi_1(t)$, $\phi_2(t)$, $\psi_1(x)$, and $\psi_2(x)$ are zero and the maximum numerical error and convergence order for $\bar{T} = 2$ are presented in Tab. 7. As it is obvious, by halving the space and time step, maximum numerical error decreases and the convergence order tends to $O(h)$ as expected. As reported in Tab. 7, the average relative error of the maximum numerical error and the convergence order at $Kn = 10$ is almost zero and the obtained numerical results are in good agreement with that of Ji *et al* [28]. The temperature profile for different values of α at $Kn=10$ when $t=200$ ps are shown in Fig. 3. As it is seen in Fig. 3(a), when $t = 200ps$, for α being 0.3, 0.5, 0.7 and 0.9, the maximum temperature is respectively, 304.8, 305.4, 305.5 and 305.6 K. Also, Fig. 3(b) demonstrates the temperature distribution at $X = 7.5nm$ for different values of α and $Kn=10$. Evidently, for α being 0.7 and 0.9 there exist oscillations at the beginning of the plot that indicates temperature instability.

4.5. Verification: Case four

For the fourth case of verification, the heat transfer at a one-dimensional slab without a heat source considering the Dirichlet boundary condition, as shown in Fig. 1 (d), is studied. The case is investigated for different values of the Knudsen numbers and the obtained results are compared with the data available from Basirat and Ghazanfarian [34]. Here, the governing equation

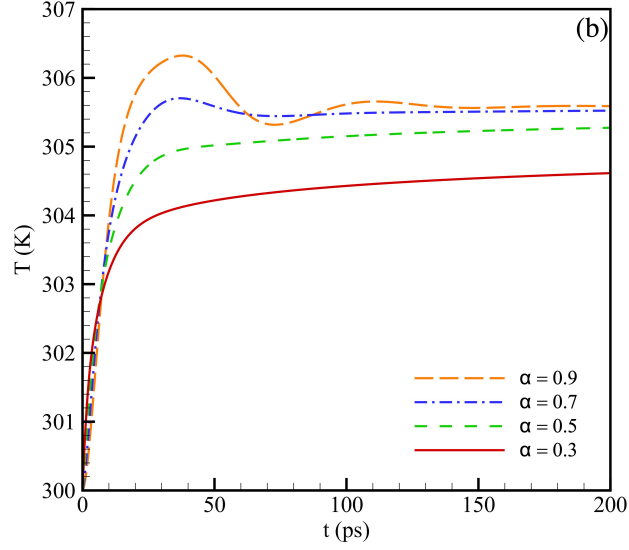
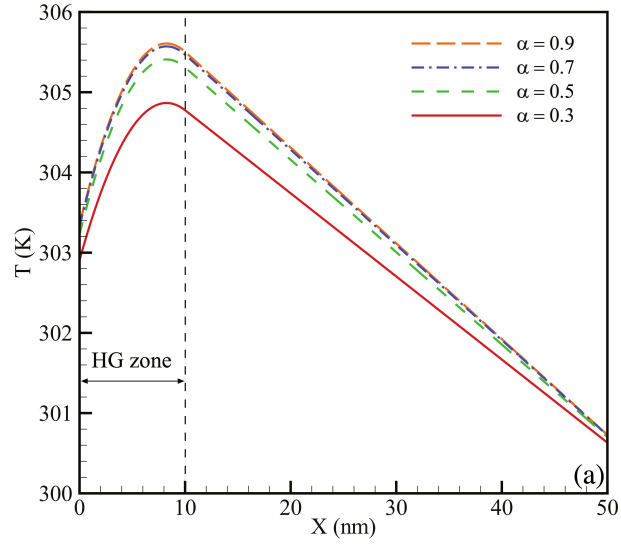


Figure 3: a) Temperature distribution for the case three of verification at $t=200$ ps, (b) temporal variation of temperature distribution at $X=7.5$ nm and $Kn=10$.

Table 7: The maximum value of the numerical error and the convergence order for $Kn = 10$

Ji et al. [28]		Present results		h	α
$H_\infty(h)$	$Rate_2$	$H_\infty(h)$	$Rate_2$		
	1.460×10^{-3}		1.460×10^{-3}	0.05	0.3
1.099	6.816×10^{-4}	1.099	6.816×10^{-4}	0.025	
1.063	3.263×10^{-4}	1.063	3.263×10^{-4}	0.0125	
1.000	1.632×10^{-4}	1.000	1.632×10^{-4}	0.00625	
	1.571×10^{-3}		1.571×10^{-3}	0.05	0.5
1.066	7.504×10^{-4}	1.066	7.504×10^{-4}	0.025	
0.983	3.797×10^{-4}	0.983	3.797×10^{-4}	0.0125	
1.002	1.896×10^{-4}	1.002	1.896×10^{-4}	0.00625	
	1.644×10^{-3}		1.644×10^{-3}	0.05	0.7
1.021	8.100×10^{-4}	1.021	8.100×10^{-4}	0.025	
1.004	4.040×10^{-4}	1.004	4.040×10^{-4}	0.0125	
1.001	2.018×10^{-4}	1.001	2.018×10^{-4}	0.00625	

is Eq. 10 as well. Also the boundary and initial conditions are,

$$\begin{aligned}
 u(0, t) &= (T_w - T_0) / T_0, \quad 0 < t \leq \bar{T} \\
 u(1, t) &= 0, \quad 0 < t \leq \bar{T} \\
 u(x, 0) &= 0, \quad u_t(x, 0) = 0, \quad 0 \leq x \leq 1.
 \end{aligned} \tag{39}$$

We have considered $T_0=300$ K and $T_w=360$ K. The non-dimensional temperature $U = \frac{T-T_0}{T_w-T_0}$ for $Kn=1$ is plotted in Fig. 4. The comparison between the obtained non-dimensional temperature profile and the data available from the Fourier, the BDE equations, and the DPL models [34], when $Kn=1$ and $\bar{T} = 2$, is carried out. We have taken $\alpha \approx 1$ in our developed fractional DPL scheme. Fig. 4 presents an appropriate consistency with our results and the one appeared in [34]. The results present a sudden drop in temperature in the temperature distribution profile. So the obtained results present better consistency with that of the BDE model in points near to the right boundary. The average relative error between our results and the one obtained by Basirat *et al.* when $Kn=1$, $\bar{T} = 2$, is less than 3% and 5%, respectively, for $B=0.01$ and $B=0.05$.

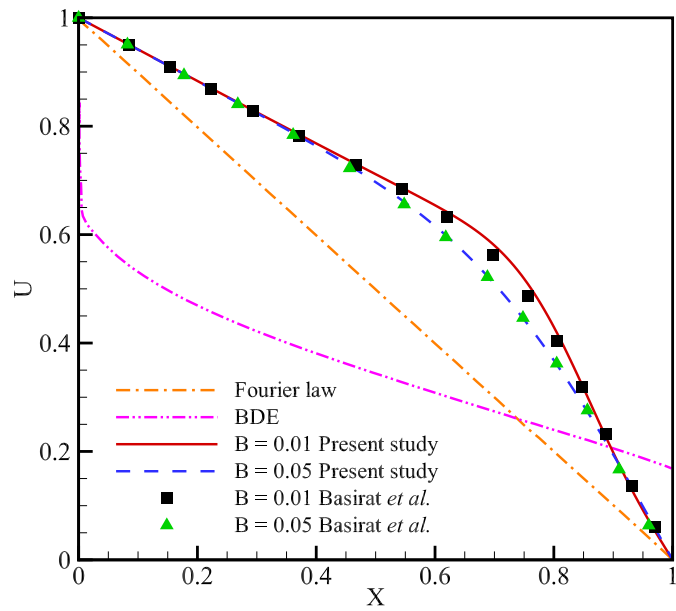


Figure 4: Comparison of the normalized temperature distribution using the Fourier's law, the BDE model, the DPL model [34], and the fractional DPL model at $Kn = 1$ and $\bar{T} = 2$.

4.6. Verification: Case five

As Fig.1 (e) suggests, the verification case number five deals with investigation of the one-dimensional silicon slab without heat source, including the temperature jump boundary condition. The results are verified with the data in [15]. Here, the initial temperature of the silicon slab is $T_0=300$ K and its length is $L_z=1000$ nm. As there exists no heat source, the characteristic length is equal to the slab length. Also, the thermal properties are presented in Tab. 6. In order to investigate the temperature profile in the silicon slab, the left temperature is increased up to $T_w=360$ K while the right boundary is kept at the environment temperature. As previously mentioned, the value of parameters B and λ along with the order of the fractional DPL model α , for each time, should be found such that the results obtained from the fractional DPL coincides with that of the Boltzmann equation. Determining several different constants for various cases is not desirable as using them is not easy. Here, the following parameters for B and λ are obtained,

$$\begin{aligned}
 B &= \begin{cases} 0.1t [\Gamma(1 + \alpha)]^{-1/\alpha}, & t \leq [\Gamma(1 + \alpha)]^{1/\alpha} \\ 0, & t > [\Gamma(1 + \alpha)]^{1/\alpha} \end{cases} \\
 \lambda &= \begin{cases} 0.7t [\Gamma(1 + \alpha)]^{-1/\alpha}, & t \leq 0.1 [\Gamma(1 + \alpha)]^{1/\alpha} \\ 0.5, & t > 0.1 [\Gamma(1 + \alpha)]^{1/\alpha} \end{cases} \quad (40)
 \end{aligned}$$

Also, the parameter $\alpha=0.975$ is found to show better consistency of the results. As it is obvious, reaching the steady state, B and λ become constant. Due to slow penetration of the heat for case $Kn=0.1$, the non-dimensional temperature distributions for $\bar{T}=1$, $\bar{T}=10$, and $\bar{T}=100$ are plotted in Fig. 5. The justifiable consistency between the results calculated from fractional DPL and the available data from Shomali *et al.* [15] were found. While the average relative error between what obtained from the DPL and the Boltzmann models is about 13%, this error is less than 11% for the results calculated from the fractional DPL model and the Boltzmann equation. This suggests that the fractional DPL model along with the temperature jump boundary condition can predict more precious temperature profiles.

5. Results and discussions

The five cases of studies are presented in Fig. 1 (f)-(j). The considered heat source and the boundary conditions are similar to what exists in a real

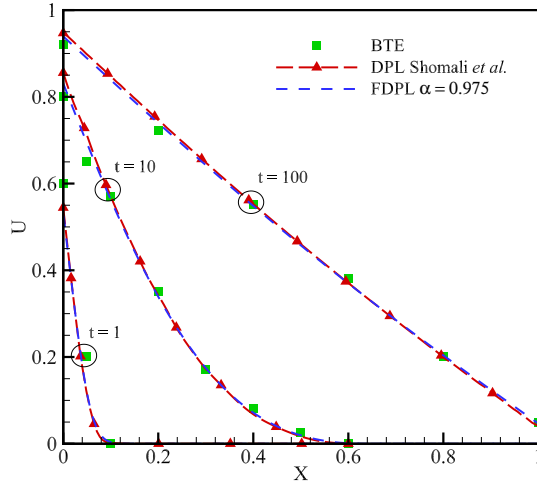


Figure 5: The non-dimensional temperature distribution obtained from Boltzmann transport equation, the DPL model [15], and fractional DPL at $Kn = 0.1$

transistor. The initial temperature of the MOSFET is taken to be the room temperature, $T_0 = 300 \text{ K}$. As Fig. 1 (f) shows, the first investigated geometry consists of a very thin silicon layer, which has a heat generation zone near the left boundary. The most generated heat is conducted towards the right boundary, and finally is discharged to the surrounding environment. This approximation is valid unless there exists no heat flow through the left boundary. In other words, due to creation of the oxide layer which has almost infinite thermal resistance on top of the MOSFET, the left boundary is considered isolating. The temperature at the right boundary is the room temperature and the heat generation zone of $Q=10^{19} \text{ W}/m^3$ and length $L_h=10 \text{ nm}$ is contemplated. The length of the transistor is $L_z=50 \text{ nm}$. This structure is investigated for two cases of (a) constant thermal properties, and (b) film-dependent thermal characteristics. The next studied geometry, Fig. 1 (g) is a transistor with a buried silicon oxide on top of the silicon layer. Other conditions in this case are similar to that of the case in Fig. 1 (f). In an additional step, the silicon channel is replaced with the newest proposed quasi-one-dimensional channels [1]. Two materials of In_4Se_3 and TiS_3 are taken into account. Such transistors shown in Figs. 1 (i) and (j) are

called quasi-one-dimensional transistors. Also, in order to investigate the functionality and reliability of these MOSFETs in comparison with the one including the silicon channel, the geometry in Fig. 1 (h) is also studied. As the Figs. 1 (h)-(j) suggests the temperature of the right boundary according to the room temperature and the temperature jump boundary condition is assumed. Also, $Q=10^{19}$ W/m³ is located at the middle of the channel. The parameters $L_h=10$ nm and $L_z=50$ nm are also utilized. In these five studied geometries, L_h is considered as the characteristic length. Also, λ and B are defined in Eq. 40. Moreover, as previously mentioned for a solid material, the thermal conductivity is $k=\rho C_p|v|\frac{\Lambda}{3}$. On the other hand, it should be noted that if the transistor length L_z is much larger than the phonon mean free-path Λ , the limited size effects appear. Under this circumstance, the mean free path of phonons is calculated as [35]:

$$\frac{1}{\Lambda_{eff}} = \frac{1}{\Lambda} + \frac{4}{L_z}. \quad (41)$$

As Λ can be replaced from $\Lambda=|v|\tau_q$, the Λ_{eff} is obtained as:

$$\frac{1}{\Lambda_{eff}} = \frac{\rho C_p |v|}{3k} + \frac{4}{L_z}. \quad (42)$$

Also, the thermal conductivity is calculated via:

$$\frac{1}{k_{film}} = \frac{1}{k} + \frac{12}{\rho C_p |v| L_z}. \quad (43)$$

Eq. 43 suggests that the silicon film thermal conductivity is always less than that of the bulk silicon. Considering the size effect in nano dimension, for certain, makes the obtained results more reliable. Also, the thermal properties of silicon, silicon dioxide, TiS₃, and In₄Se₃ are presented in Tab. 8.

5.1. Result: Cases (I) and (II)

In this section, the first case, Fig. 1 (f), is studied while the bulk and also film thermal conductivity are taken into account. Figs. 6 (a), (c), (e) show, respectively, the temperature and heat flux distributions at $t=10$, and the maximum temperature obtained from the fractional DPL model with considering the bulk thermal conductivity. Also, Figs. 6 (b), (d), (f) show the

Table 8: Thermal properties of Si [36], SiO₂ [37], TiS₃ [38, 39], and In₄Se₃ [40].

	$ v $ (ms ⁻¹)	k (Wm ⁻¹ K ⁻¹)	ρC_p (Jm ⁻³ K ⁻¹)	Λ (nm)
Si	3000	150	1.5×10^6	100
SiO ₂	5900	1.4	1.75×10^6	0.4
TiS ₃	3535	8.28	3.877×10^6	1.81
In ₄ Se ₃	2010	0.9	1.505×10^6	0.892

results when the film thermal characteristics are contemplated. As it is seen in Figs. 6 (a) and (b), considering size dependency of the thermal properties, changes the temperature distribution such that the temperature jump at the right boundary decreases. This decrement is due to the decrease of thermal conductivity from $150Wm^{-1}K^{-1}$ to $16.67Wm^{-1}K^{-1}$ which itself, results in reduction of the Knudsen number from 10 to 1.5. So, the temperature jump controlling term, ΛKn also decreases. As the thermal conductivity decreases, the total time in which all the transistors are affected by the heat generation zone increases. Consequently, the time for reaching the steady state condition augments. Moreover, Fig. 6 (a) suggests that as the α increases, the temperature jump at the right boundary decreases, and the whole temperature distribution plot is placed lower. This trend is recognizable for the heat flux plot. Further, for a silicon transistor with size dependent thermal characteristics where the Knudsen number decreases by 1.1, the temperature jump at the right boundary is not sensible for all values of α . Increasing α , the penetration heat decreases. In other words, when α reaches 1, the heat penetration becomes smaller. As the temperature jump reduces, for the similar time, the temperature in all positions takes higher values. The heat flux also obeys such behavior. It is worthy to mention that when the transistor size becomes much larger than the phonon mean free-path, the difference between the results appearing from taking film dependent or constant bulk thermal properties vanishes. It is obvious that the reason is reaching the bulk limit by increasing the system size. Additionally, the time dependency of the peak temperature rise is presented in Figs. 6 (e) and (f). It is found that the maximum temperature obtained from the fractional DPL model is always larger when the size dependent thermal properties are considered. For example, at $t=40$ ps and when $\alpha \simeq 1$, the maximum temperature rise is 32 K and 112 K, respectively for constant bulk and size-dependent ther-

mal characteristics. On the other hand, the maximum temperature for the same system when considering both size and temperature dependent thermal properties, calculated from the common DPL model, is reported as 55 K and 112 K [15]. Figure 6 (e) also shows that when α is equal to 0.7, 0.9, and almost 1, oscillations appear in maximum temperature plot which present the negative-bias temperature instability (NBTI) [41, 42, 43]. This phenomenon identified as the short-memory principle is observed in the works [29, 44]. In consequence, taking into account the bulk thermal properties for the film structures, notably underestimates the obtained temperature profiles and the peak temperature rise. So, it is important to consider the size-dependent thermal properties of the film structures, in order to calculate a more accurate temperature distribution.

In the following, the results for the second case, Fig. 1 (g), will be presented. Here, the heat generation zone is considered at the top of the transistor, at a place where there exists silicon dioxide. Using SiO_2 makes the effective electrical capacitance reduce, and it increases the operating speed [45]. On the other hand, the temperature increases in the oxide layer which is due to the lower thermal conductivity coefficient of SiO_2 relative to the Si, can cause the transistor failure. In SiO_2/Si transistors, the silicon layer with high thermal conductivity increases the heat transfer, and helps the generated heat in the heating source to leave. So, the buried oxide layer operates like a cage for the heat such that the heat tends to flow from the silicon body. Figures. 7 (a) and (b) show the temperature profile for the SiO_2/Si transistors with bulk and size-dependent thermal properties. It is obvious that the low thermal conductivity of the SiO_2 has caused the temperature increase remarkably such that the temperature everywhere in the SiO_2/Si transistor is larger than that of Si transistor without any SiO_2 layer. At the same time, considering the limited size effect reduces the thermal conductivity of the SiO_2 from $1.4\text{Wm}^{-1}\text{K}^{-1}$ to $1.35\text{Wm}^{-1}\text{K}^{-1}$. This also causes the Knudsen number to decrease from 0.04 to 0.0394. So, considering the size-effects makes the thermal conductivity and the Knudsen number in the SiO_2 layer to change slightly. Consequently, As Figs. 7 (a) and (b) show, the low thermal conductivity of SiO_2 also makes the temperature distribution behavior very similar in SiO_2 parts of the transistor with both different defined thermal properties. Also, taking into account the size-effects in the silicon part of the transistor results in prominent decrement of thermal conductivity and Knudsen number, subsequently, from $150\text{Wm}^{-1}\text{K}^{-1}$ to $16.67\text{Wm}^{-1}\text{K}^{-1}$ and from 10 to 1.1. Accordingly, the temperature profile plots for the two cases with

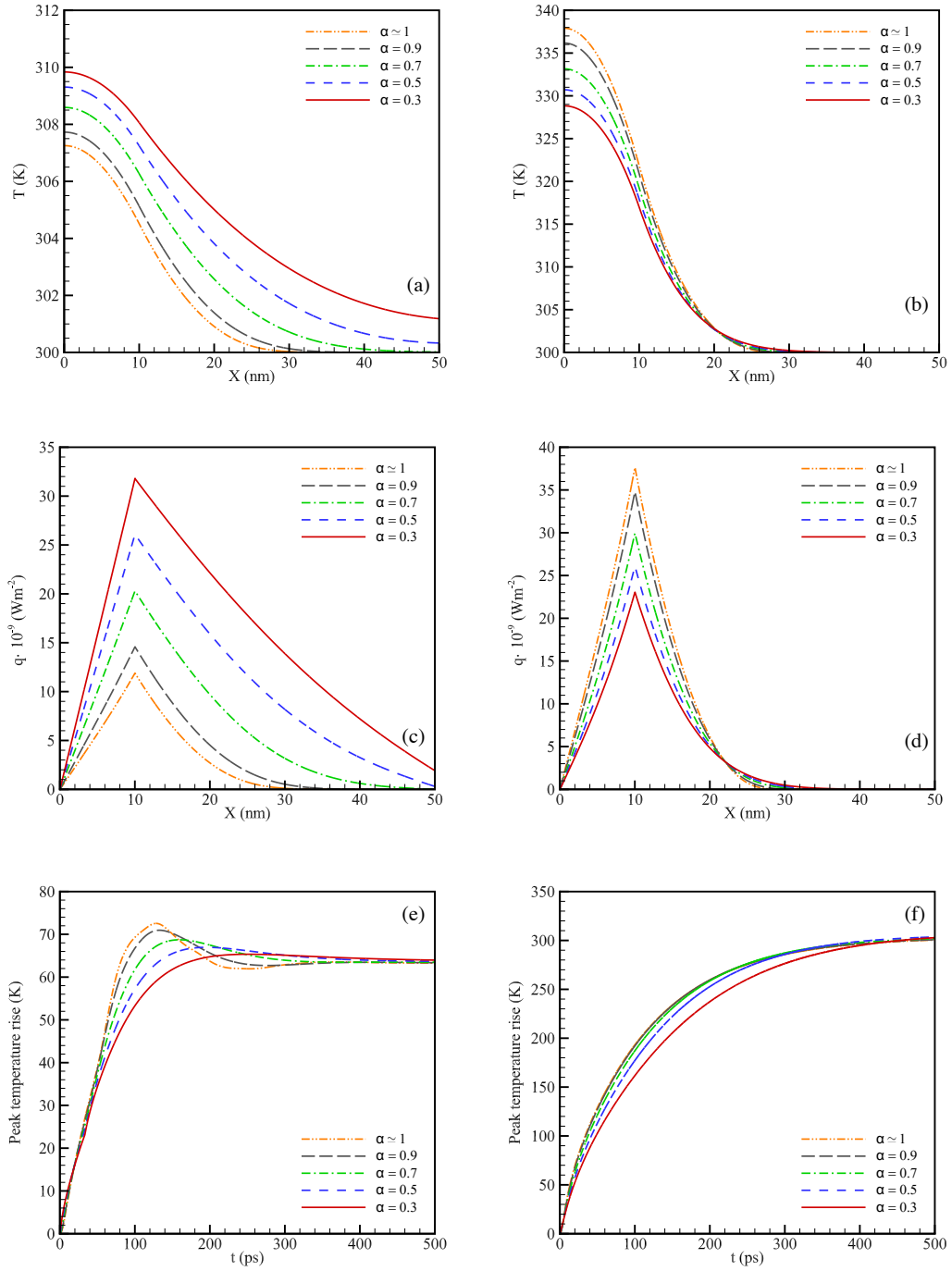


Figure 6: (a), (c), (e), respectively, the temperature and heat flux distributions for case (I) at $t=10$ ps, and variation of the peak temperature in the transistors with bulk thermal conductivity. (b), (d), (f), the same as (a), (c) and (e) but for systems with the film thermal conductivity.

different bulk or size-dependent thermal properties are completely dissimilar. Besides, the size-dependent thermal specificities give rise to increment of the temperature at two-layer contact area, such that the temperature value for $\alpha \simeq 1$ increases from 301.8 K to 310.1 K.

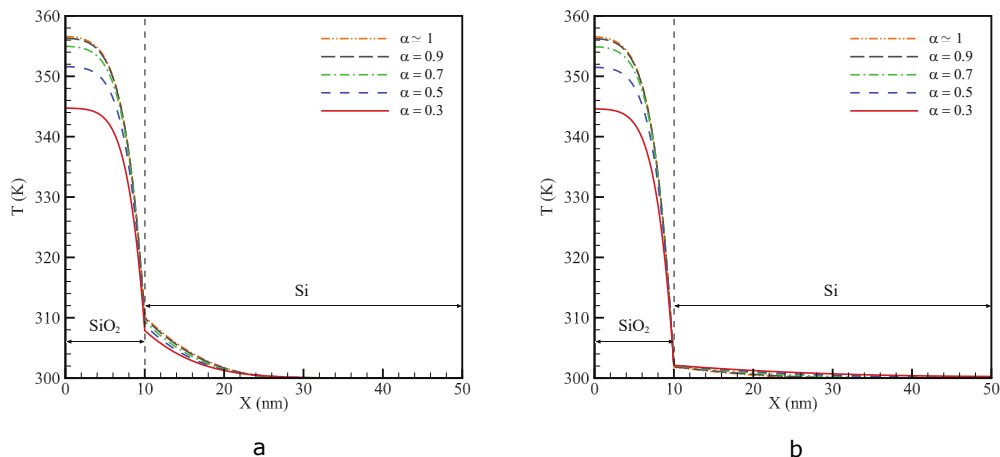


Figure 7: Temperature distribution obtained from the fractional DPL model for the case (II) at 10 ps, (a) film properties, (b) bulk properties.

5.2. Result: Cases III-V

In this section, the obtained results for the cases presented in Figs. 1 (h), (i), and (j), while considering the film-dependent thermal properties, are discussed. As previously mentioned, the heat generation zone is considered at the center of the transistor. In Figs. 8 (a), (c), and (e), the temperature distribution profiles obtained from fractional DPL model, respectively, for silicon, TiS_3 , and In_4Se_3 at $t=10$ ps are given. It is obvious that the temperature of the silicon transistor presents a higher value all over the transistor relative to the TiS_3 and In_4Se_3 temperature, for all values of α . Also, as α augments, the temperature jump value at the right boundary decreases while the temperature increases. Also, in similarity to the previously studied geometries, with α reduction, the heat penetration over the transistor length enhances. For $\alpha \simeq 1$, the maximum temperature rise for the silicon transistor at $t=10$, is 24.72 K. Further, as the Knudsen number is 1.1, reducing α and increasing the temperature jump at the right boundary, the peak

temperature in early times ($t \leq 3.28$ ps), has larger values. The temperature distribution profiles of TiS_3 and In_4Se_3 , obtained from the fractional DPL model at $t=10$ ps for different values of α , are respectively shown in Figs. 8 (c) and (e). It is obtained that for the same values of α , the temperature profile for In_4Se_3 MOSFET is placed in a higher temperature range relative to TiS_3 . This can be justified as the Knudsen number, the temperature jump, and the heat flux phase lag for In_4Se_3 ($\text{Kn}=0.083$ and $\tau_q=0.414$ ps) are smaller than that of TiS_3 ($\tau_q=0.447$ ps and $\text{Kn}=0.158$). Also as Fig. 8 (a) suggests, due to the larger value of the Knudsen number and the temperature jump for the silicon FET relative to the geometries presented in Fig. 1 (i) and (j), the temperature distribution around boundaries, increases in value with α reduction. Also comparing Figs. 8 (a), (c), and (e), one finds the heat penetration in the silicon MOSFET is higher than in titanium trisulfide and tetraindium triselenide MOSFETs. Further, the localized heating is also obvious. The maximum temperature time-variation plot of TiS_3 and In_4Se_3 are demonstrated in Figs. 8 (d) and (f). It is shown that the peak temperature rise when $\alpha \simeq 1$, is 19.63 and 61.48, respectively, for TiS_3 and In_4Se_3 . Conclusively, as the results for the maximum temperature of Si, TiS_3 and In_4Se_3 confirm, the TiS_3 FET having the least peak temperature rise, has the highest reliability. In other words, the formed hot spot in the titanium trisulfide FET is cooler than the other two studied MOSFETs. So, the TiS_3 FET is suggested as the suitable replacement for the old-fashioned silicon transistors.

6. Conclusions

Due to the need for increasing the performance of electronic devices, reducing the sizes of these systems is inevitable. On the other hand, as the system characteristic length decreases, the Fourier law loses its validity. Instead, atomistic methods such as the molecular dynamics (MD) simulation or the phonon Boltzmann equation (PBE) are utilized. These methods have high computational costs, and also owing to their complexity, there exist limitations for applying them in complex structures. So, researchers with the help of precious results obtained from the atomistic methods can provide new models for modified classical equations like the DPL model. The new proposed models can produce accurate atomistic results with lower computational costs. In this regard, there have been many attempts for employing the DPL model to nanoscale problems. Recently, the combination of the frac-

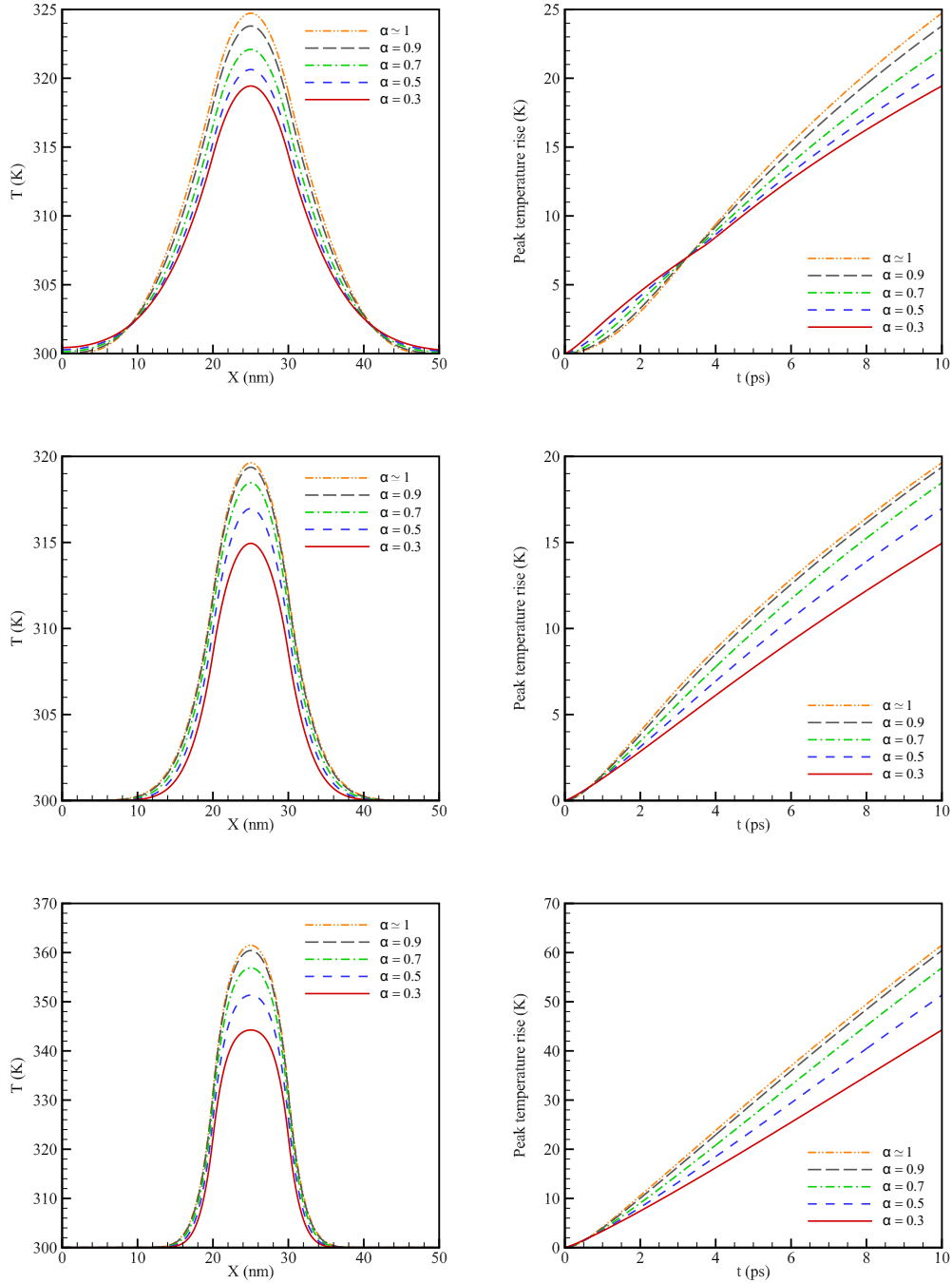


Figure 8: (a), (c) and (e), the temperature distribution at $t=10$, respectively for, silicon, TiS_3 , and In_4Se_3 quasi-one-dimensional transistors. (b), (d), and (f), the variation of the peak temperature in the, respectively, silicon, TiS_3 , and In_4Se_3 transistors with film thermal properties.

tional calculus and the phase lag theory, leading to more accurate results, has been the center of interest. On the other hand, the newly proposed TiS_3 , and In_4Se_3 FETs are obtained to be suitable candidates for the silicon channel replacements.

In the present study, the fractional DPL model discretized using the finite difference scheme is utilized to investigate the one-dimensional MOSFETs and quasi-one-dimensional FETs. To fulfill this aim, first, verification of the developed fractional DPL model had been performed. Then the elaborated fractional DPL method is applied for the newly quasi-one-dimensional suggested transistors while the thermal properties are taken to be size-dependent. It is obtained that considering size-dependent thermal characteristics make the peak temperature rise to increase, up to 250%. Also, it has reduced the temperature jump at the right boundary. The maximum temperature of the hotspot. The reliability has been investigated for the FET containing new two-dimensional proposed materials with quasi-one-dimensional band gap, named as TMT. It has been obtained that among the studied FETs, the transistor with titanium trisulfide channel presents the least temperature increase (19.63 K). Hence, TiS_3 can be suggested as the noteworthy substitution of the silicon channel.

References

- [1] P. V. Galiy, M. Randle, A. Lipatov, L. Wang, S. Gilbert, N. Vorobeva, A. Kumar, C.-P. Kwan, J. Nathawat, B. Barut, et al., Building the quasi one dimensional transistor from 2d materials, 2019 IEEE 2nd Ukraine Conference on Electrical and Computer Engineering (UKRCON) (2019) 679–682.
- [2] . Kumar, M. M. Tripathi, R. Chaujar, Comprehensive analysis of sub-20 nm black phosphorus based junctionless-recessed channel mosfet for analog/rf applications, Superlattices and Microstructures 116 (2018) 171–180.
- [3] Z. Shomali, R. Asgari, Effects of low-dimensional material channels on energy consumption of nano-devices, International Communications in Heat and Mass Transfer 94 (2018) 77–84.
- [4] M. Wimmer, I. Adagideli, S. Berber, D. Tománek, K. Richter, Spin

currents in rough graphene nanoribbons: Universal fluctuations and spin injection, *Physical review letters* 100 (17) (2008) 177207.

- [5] A. Patra, C. S. Rout, Anisotropic quasi-one-dimensional layered transition-metal trichalcogenides: synthesis, properties and applications, *RSC Advances* 10 (2020) 36413–36438.
- [6] A. Lipatov, M. J. Loes, H. Lu, J. Dai, P. Patoka, N. S. Vorobeva, D. S. Muratov, G. Ulrich, B. K stner, A. Hoehl, et al., Quasi-1d TiS_3 nanoribbons: mechanical exfoliation and thickness-dependent raman spectroscopy, *ACS nano* 12 (12) (2018) 12713–12720.
- [7] D. Y. Tzou, A unified field approach for heat conduction from macro-to micro-scales, *J. Heat Transfer* 117 (1) (1995) 8–16.
- [8] D. Tzou, K. Chiu, Temperature-dependent thermal lagging in ultrafast laser heating, *International Journal of Heat and Mass Transfer* 44 (9) (2001) 1725–1734.
- [9] J. Ghazanfarian, Z. Shomali, Investigation of dual-phase-lag heat conduction model in a nanoscale metal-oxide-semiconductor field-effect transistor, *International Journal of Heat and Mass Transfer* 55 (21-22) (2012) 6231–6237.
- [10] J. Ghazanfarian, A. Abbassi, Investigation of 2d transient heat transfer under the effect of dual-phase-lag model in a nanoscale geometry, *International Journal of Thermophysics* 33 (3) (2012) 552–566.
- [11] R. Samian, A. Abbassi, J. Ghazanfarian, Thermal investigation of common 2d fets and new generation of 3d fets using boltzmann transport equation in nanoscale, *International Journal of Modern Physics C* 24 (9) (2013) 1350064.
- [12] R. Samian, A. Abbassi, J. Ghazanfarian, Transient conduction simulation of a nano-scale hotspot using finite volume lattice boltzmann method, *International Journal of Modern Physics C* 25 (4) (2014) 1350103.
- [13] M. Moghaddam, J. Ghazanfarian, A. Abbassi, Implementation of dpl-dd model for the simulation of nanoscale mos devices, *IEEE Transactions on Electron Devices* 61 (2014) 3131–3138.

- [14] Z. Shomali, A. Abbassi, Investigation of highly non-linear dual-phase-lag model in nanoscale solid argon with temperature-dependent properties, *International Journal of Thermal Sciences* 83 (2014) 56–67.
- [15] Z. Shomali, J. Ghazanfarian, A. Abbassi, Effect of film properties for non-linear dpl model in a nanoscale mosfet with high-k material: $ZrO_2/HfO_2/La_2O_3$, *Superlattices and Microstructures* 83 (2015) 699–718.
- [16] Z. Shomali, A. Abbassi, J. Ghazanfarian, Development of non-fourier thermal attitude for three-dimensional and graphene-based mos devices, *Applied Thermal Engineering* 104 (2016) 616–627.
- [17] J. Ghazanfarian, Z. Shomali, A. Abbassi, Macro- to nanoscale heat and mass transfer: The lagging behavior, *International Journal of Thermophysics* 36 (2015) 1416–1467.
- [18] r. Saghatchi, J. Ghazanfarian, A novel sph method for the solution of dual-phase-lag model with temperature-jump boundary condition in nanoscale, *Applied Mathematical Modelling* 39 (2015) 1063–1073.
- [19] Z. Shomali, B. Pedar, J. Ghazanfarian, A. Abbassi, Monte-carlo parallel simulation of phonon transport for 3d silicon nano-devices, *International Journal of Thermal Sciences* 114 (2017) 139–154.
- [20] Z. Shomali, J. Ghazanfarian, A. Abbassi, 3-d atomistic investigation of silicon mosfets, in: *In Proceedings of CHT-17 ICHMT International Symposium on Advances in Computational Heat Transfer*. Begel House Inc, 2017, pp. 1385–1401.
- [21] M. Jamshidi, J. Ghazanfarian, Dual-phase-lag analysis of cnt-mos2-zro2-sio2-si nano-transistor and arteriole in multi-layered skin, *Applied Mathematical Modelling* 60 (2018) 490–507.
- [22] O. Zobiri, A. Atia, M. Arıcı, A three-dimensional analysis of heat transfer based on mesoscopic method in nanoscale si-mosfet and gr-fet, *Superlattices and Microstructures* (2021) 107123.
- [23] C. M., M. F, A new dissipation model based on memory mechanism, *Pure and Applied Geophysics* 91 (1971) 134–147.

- [24] C. M., M. F, Linear model of dissipation in anelastic solids, *Rivista del Nuovo cimento* 1 (1971) 161–198.
- [25] C. M., Vibrations on an infinite viscoelastic layer with a dissipative memory, *Journal of the Acoustical Society of America* 56 (1974) 897–904.
- [26] H. H. Sherief, A. El-Sayed, A. Abd El-Latief, Fractional order theory of thermoelasticity, *International Journal of Solids and structures* 47 (2) (2010) 269–275.
- [27] T. Mishra, K. Rai, Numerical solution of fractional heat conduction equation for analysis of thermal propagation, *Applied Mathematics and Computation* 273 (2016) 1006–1017.
- [28] C.-C. Ji, W. Dai, Z.-Z. Sun, Numerical method for solving the time-fractional dual-phase-lagging heat conduction equation with the temperature-jump boundary condition, *Journal of Scientific Computing* 75 (3) (2018) 1307–1336.
- [29] C.-C. Ji, W. Dai, Z.-Z. Sun, Numerical schemes for solving the time-fractional dual-phase-lagging heat conduction model in a double-layered nanoscale thin film, *Journal of Scientific Computing* 81 (3) (2019) 1767–1800.
- [30] J. Ghazanfarian, A. Abbassi, Effect of boundary phonon scattering on dual-phase-lag model to simulate micro-and nano-scale heat conduction, *International Journal of Heat and Mass Transfer* 52 (15-16) (2009) 3706–3711.
- [31] W. Dai, F. Han, Z. Sun, Accurate numerical method for solving dual-phase-lagging equation with temperature jump boundary condition in nano heat conduction, *International Journal of Heat and Mass Transfer* 64 (2013) 966–975.
- [32] W. Dai, R. Nassar, An approximate analytic method for solving 1d dual-phase-lagging heat transport equations, *International journal of heat and mass transfer* 45 (8) (2002) 1585–1593.

- [33] M. Caputo, Linear models of dissipation whose q is almost frequency independent, *Geophysical Journal International* 13 (5) (1967) 529–539.
- [34] H. Basirat, J. Ghazanfarian, P. Forooghi, Implementation of dual-phase-lag model at different knudsen numbers within slab heat transfer, *Proc. of Int. Conf. on Modeling and Simulation (MS06)* (2006) 895–899.
- [35] P. K. Schelling, S. R. Phillpot, P. Keblinski, Comparison of atomic-level simulation methods for computing thermal conductivity, *Physical Review B* 65 (14) (2002) 144306.
- [36] R. Yang, G. Chen, M. Laroche, Y. Taur, Simulation of nanoscale multi-dimensional transient heat conduction problems using ballistic-diffusive equations and phonon boltzmann equation, *J. Heat Transfer* 127 (3) (2005) 298–306.
- [37] K. Goodson, M. Flik, Effect of microscale thermal conduction on the packing limit of silicon-on-insulator electronic devices, *IEEE Transactions on Components Hybrids and Manufacturing Technology* 15 (5) (1992) 715–722.
- [38] M. Abdulsalam, D. P. Joubert, Structural and electronic properties of Mx_3 ($\text{M} = \text{Ti, Zr and Hf}$; $\text{X} = \text{S, Se, Te}$) from first principles calculations, *The European Physical Journal B* 88 (7) (2015) 1–11.
- [39] J. Zhang, X. Liu, Y. Wen, L. Shi, R. Chen, H. Liu, B. Shan, Titanium trisulfide monolayer as a potential thermoelectric material: a first-principles-based boltzmann transport study, *ACS applied materials & interfaces* 9 (3) (2017) 2509–2515.
- [40] S. D. Luu, A. R. Supka, V. H. Nguyen, D.-V. N. Vo, N. T. Hung, K. T. Wojciechowski, M. Fornari, P. Vaqueiro, Origin of low thermal conductivity in In_4Se_3 , *ACS Applied Energy Materials* 3 (12) (2020) 12549–12556.
- [41] M. Liao, Z. Gan, New insight on negative bias temperature instability degradation with drain bias of 28 nm high-k metal gate p-mosfet devices, *Microelectronics Reliability* 54 (11) (2014) 2378–2382.

- [42] A. T. Krishnan, V. Reddy, S. Chakravarthi, J. Rodriguez, S. John, S. Krishnan, Nbti impact on transistor and circuit: models, mechanisms and scaling effects [mosfets], in: IEEE international electron devices meeting 2003, 2003, pp. 14–5.
- [43] B. C. Paul, K. Kang, H. Kufuoglu, M. A. Alam, K. Roy, Impact of nbti on the temporal performance degradation of digital circuits, IEEE Electron Device Letters 26 (8) (2005) 560–562.
- [44] I. Podlubny, Fractional differential equations: an introduction to fractional derivatives, fractional differential equations, to methods of their solution and some of their applications, Elsevier, 1998.
- [45] P. G. Sverdrup, Y. Sungtaek Ju, K. E. Goodson, Sub-continuum simulations of heat conduction in silicon-on-insulator transistors, J. Heat Transfer 123 (1) (2001) 130–137.